

# Simulation study on a novel solid–gas coupling hydrogen storage method for photovoltaic hydrogen production systems

Yuhang Wang<sup>a</sup>, Hui Dai<sup>a</sup>, Zeqi Chen<sup>a</sup>, Suoying He<sup>a</sup>, Wenlong Wang<sup>a</sup>, Ming Gao<sup>a,b,\*</sup>

<sup>a</sup> Shandong Engineering Research Center for High-efficiency Energy Storage and Hydrogen Energy Utilization, School of Energy and Power Engineering, Shandong University, Jinan, Shandong 250061, China

<sup>b</sup> Shenzhen Research Institute of Shandong University, Shenzhen, Guangdong, 518057, China

## ARTICLE INFO

### Keywords:

Photovoltaic hydrogen production system  
Solid-gas coupling hydrogen storage  
Metal hydride  
Phase change material  
Numerical simulation

## ABSTRACT

Compressed hydrogen storage in photovoltaic hydrogen production systems faces several challenges, including limitations in storage volume, compression energy consumption and safety concerns. To improve the comprehensive hydrogen storage performance, this study develops a novel solid–gas coupling hydrogen storage method that combines metal hydride and phase change material (MH-PCM). Firstly, a vertical MH-PCM solid storage model considering the natural convection effect is proposed and investigated. Building upon this model, the solid–gas coupling hydrogen storage is constructed and integrated into the photovoltaic hydrogen production system to evaluate its comprehensive storage performance. Results reveal that considering natural convection leads to an approximately 12.7 % increase in the average storage rate, but is also accompanied by an uneven storage process. To address this unevenness and further enhance the storage rate, it's advisable to focus on structural optimization at the bottom of the tank. Additionally, improving the PCM thermal conductivity and hydrogen inlet pressure (to approximately 1 MPa) are also proven effective strategies. The proposed solid–gas coupling hydrogen storage demonstrates comprehensive advantages, particularly compact size and reduced energy consumption. Furthermore, appropriately increasing the coupling ratio between solid and gaseous capacities can achieve the even smaller storage volume. These findings can provide valuable theoretical and engineering guidance for implementing such hydrogen production and storage systems.

## 1. Introduction

To combat global climate change and achieve the goals of the Paris Agreement, there is a global shift towards sustainable renewable energy production [1]. For instance, China plans to achieve a total installed capacity of over 1200 GW in wind and solar power by 2030 [2]. China, being a global leader in solar panel production and solar-generated electricity [3], will account for 40 % of the global renewable capacity by 2024, particularly in the field of distributed photovoltaic (PV) [4]. However, renewable energy generation exhibits intermittency and fluctuations, leading to a severe mismatch between energy production and demand [5]. Therefore, ensuring a highly reliable renewable energy supply is essential for achieving carbon neutrality.

A promising solution in this endeavor is the production and storage of hydrogen through water electrolysis, employing PV generators for sustainable energy. In this field, hydrogen storage technologies primarily include compressed gaseous storage, cryogenic liquid storage,

and solid storage [6]. Reports indicate that compressing hydrogen to 800 bar consumes roughly 15.5 % of its low heating value, while converting hydrogen to a liquid state requires over 30 % of its low heating value. Notably, solid storage using metal hydride exhibits much lower energy consumption, accounting for only 4–5 % of its low heating value (at approximately 20 bar) [7]. Accordingly, the parasitic power consumption and potential safety risks hazards of high-pressure gaseous storage or liquid storage significantly limit the large-scale development of hydrogen-based renewable energy systems [1,8]. However, Marino et al. [9] demonstrated that low-pressure gaseous hydrogen storage tanks are impractical, especially in public areas or residential buildings, due to their enormous space requirements. Consequently, there is an urgent need for innovative low-pressure hydrogen storage technologies to overcome these constraints and enhance energy storage efficiency.

Metal Hydride (MH) is a solid hydrogen storage method known for its remarkable material volume hydrogen storage density, reaching up to 100 kg/m<sup>3</sup>. Moreover, this method offers low storage pressure and energy consumption, making it highly attractive for potential

\* Corresponding authors.

E-mail address: [gm@sdu.edu.cn](mailto:gm@sdu.edu.cn) (M. Gao).

<https://doi.org/10.1016/j.enconman.2023.117866>

Received 19 June 2023; Received in revised form 3 November 2023; Accepted 7 November 2023

Available online 9 November 2023

0196-8904/© 2023 Elsevier Ltd. All rights reserved.

Nomenclature		Greek symbols	
$A, B$	Empirical constant of MH	$\gamma$	Adiabatic index
$A_{\text{cell}}$	Area of the electrodes, $\text{m}^2$	$\varepsilon$	Porosity
$a$	Ideal parameter of the diode	$\eta$	Efficiency, %
$b$	Boltzmann constant, J/K	$\kappa$	Permeability, $\text{m}^2$
$C$	Absorption constant, $\text{s}^{-1}$	$\mu$	Dynamic viscosity, Pa·s
$C_p$	Specific heat capacity, J/kg/K	$\nu$	Darcy's velocity, m/s
$E$	Activation energy, J/mol	$\rho$	Density, $\text{kg/m}^3$
$F$	Faraday constant, C/mol	$\nabla$	Gradient operator
$f$	Liquid mass fraction of PCM, %	<i>Subscript and superscript</i>	
$G$	Irradiance intensity, $\text{W/m}^2$	0	Initial
$G_f$	Gibbs free energy, J	100 s	100th second
$H, h$	Enthalpy, J/mol	atm	Atmosphere
$I$	Current, A	abs	Absorption
$k$	Thermal conductivity, W/m/K	com	Compressor
$k_z$	Compression constant	cell	Electrolyzer cell
$L$	Latent heat, J/kg	eff	Effective
$l$	Length	el	Electrolyzer
$m$	Mass per unit volume, $\text{kg/m}^3$	eq	Equilibrium
$N$	Number	$\text{H}_2$	Hydrogen
$n$	Amount of substance, mol	in	Inlet
$P$	Pressure, Pa	m	Melt
$Power$	Power, W	oc	Open-circuit
$q$	Electronic charge, C	ph	Photogenerated
$R$	Universal gas constant, J/mol/K	pv	Photovoltaic
$r_{\text{wall}}$	Radius of the tank, m	s, p	Series, parallel
$r_1, r_2$	Parameters of electrolyte	sat, emp	Saturated, empty
$s_1, s_2, s_3$	Parameters of electrolyte	sc	Short-circuit
$T$	Temperature, K	<i>Abbreviations</i>	
$t$	Time variable, s	MH	Metal Hydride
$t_1, t_2, t_3$	Parameters of electrolyte	MPPT	Maximum power point tracking
$U$	Convective heat transfer coefficient, $\text{W/m}^2/\text{K}$	PCM	Phase change material
$V, v$	Voltage, V	PV	Photovoltaic
$Vol$	Volume, $\text{m}^3$	PWM	Pulse Width Modulator
$W$	Flow, kg/s	UDF	User-defined function
$Z$	Compression coefficient		
$z, r$	z-axis, r-axis,		

applications and research [10]. Experimental work by Liu et al. [11] validated the efficiency of MH storage and proposed a hybrid approach combining MH and compressed gaseous storage. However, the MH absorption is accompanied by an exothermic process, necessitating external thermal management to maintain optimal storage conditions in the MH tank [12]. To address this challenge, researchers have proposed various strategies to enhance heat transfer, including adding fins [13], arranging heat pipes [12], and improving the structure of the heat exchanger [14]. These methodologies collectively aim to enhance the heat exchange efficiency between the MH tank and external coolant, ultimately improving the hydrogen storage rate. However, the generated heat during the MH absorption process is typically absorbed by the coolant and dissipated into the surrounding air, leading to increased energy consumption [15]. Consequently, research focuses on energy-saving optimization techniques tailored to MH hydrogen storage.

Phase change material (PCM) is an increasingly promising solution for heat storage due to its high latent heat capacity and low noise characteristics [16]. Researchers have found that PCM can effectively store heat generated during the MH absorption process, and serves as a heat source during the MH desorption process, enabling heat recycling in the MH absorption/desorption cycle [17]. Mellouli et al. [18] proposed a MH-PCM coupled hydrogen storage tank, and developed a heat and mass transfer model, demonstrating the effectiveness of thermal coupling through numerical simulations. Mghari et al. [19] emphasized

that the thermal conductivity and latent heat of PCM are important factors affecting the hydrogen storage rate of the MH-PCM tank. Besides, Tong et al. [20] found that the thermal conductivity of MH also impacts hydrogen storage performance significantly. To improve hydrogen storage efficiency, numerous researchers have focused on enhancing the heat and mass transfer of the MH-PCM tank by incorporating materials of aluminum and copper foam in the PCM domain [21], integrating coils in MH domain [20], and optimizing the PCM shape and spatial positioning within the MH-PCM tank [22].

In summary, previous studies mainly concentrated on optimizing heat transfer in the MH-PCM tank. However, it's worth noting that the PCM density changes during phase transformation, and the natural convection effect driven by gravity impacts the melting process [23,24]. Fang et al. [25] revealed that heat conduction and natural convection exhibit varying levels of influence during different stages of the PCM melting, with natural convection being the primary factor determining the melting duration. Therefore, it is crucial to account for the impact of natural convection on the hydrogen storage performance of the MH-PCM tank, an aspect usually overlooked in existing literature.

Additionally, integrated research on PV hydrogen production systems is essential due to the limited capacity of individual hydrogen storage tanks. However, existing studies have primarily focused on integrating gaseous hydrogen storage tanks [26,27]. It's worth noting that gaseous hydrogen storage not only requires significant space but

**Table 1**

The summary of the above literatures.

Reference	Pros	Cons
[9]	Gaseous hydrogen storage is convenient and widely used in PV hydrogen production systems.	Impractical in public areas or residential buildings due to the enormous space, high pressure and energy consumption.
[7,10]	Highlighted the advantages of storage density and safety of solid-state MH storage.	Lacked thorough discussions of the practical challenges with MH storage applications.
[11]	Confirmed the efficiency of MH storage through experimental validation and proposed a hybrid storage approach.	Lacked specific details on thermal management enhancements and quantitative the comprehensive performance assessments.
[12–14]	Enhanced heat exchange efficiency within the MH tank, improving hydrogen storage rates.	The heat generated during the MH absorption process was commonly dissipated into the air, resulting in higher energy consumption.
[18–22]	Explored energy-saving benefits of MH-PCM coupling storage and revealed key factors.	The impact of gravity-induced natural convection was rarely considered.
[23–25]	Analyzed the critical role of natural convection and its impact mechanism on the phase transition process.	Lacked specific studies or application examples addressing the impact of natural convection on PCM-MH storage tanks.
[26,27]	Integrated gaseous hydrogen storage into PV systems and highlights its pivotal role.	Recommended exploring alternative methods to replace gaseous hydrogen storage, particularly in large-scale applications.
[28,29]	The thermal effects of MH in PV systems can fulfill the thermal demands of various users.	Challenges in managing variable loads and addressing heat dissipation wastage.
[30]	Combined PCM and MH to establish an energy storage system for concentrated solar energy power plants.	Not considering the comprehensive process of PV hydrogen production and storage.

also incurs high energy consumption due to the need for high pressure storage. Recognizing these limitations, Bellos et al. [27] recommended exploring alternative methods to replace gaseous hydrogen storage, particularly in large-scale applications.

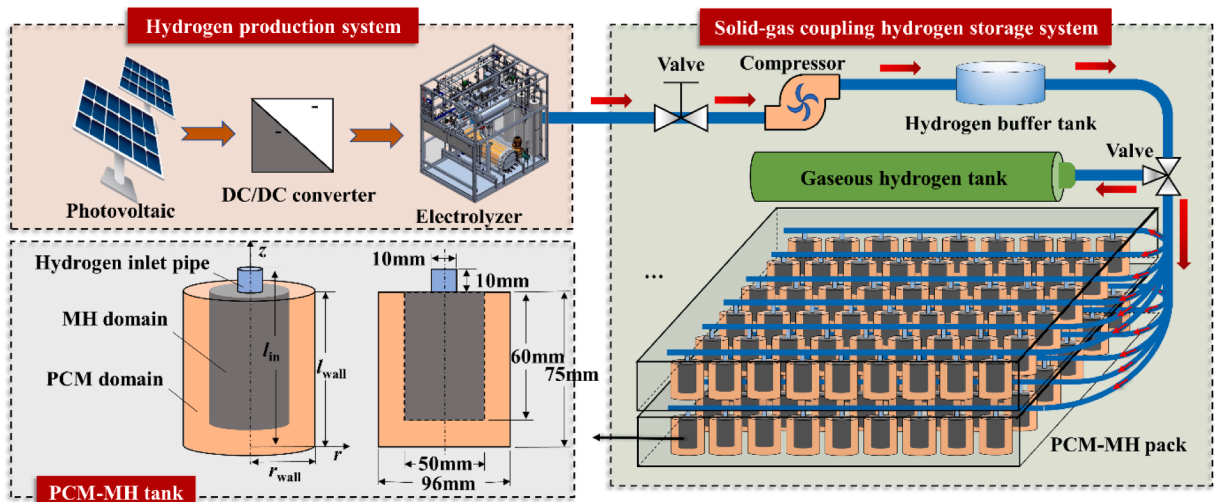
Recently, MH hydrogen storage has gradually been used in PV hydrogen production systems. For instance, Sharma et al. [28] found that the thermal effects arising from the MH adsorption and desorption reaction can fulfill over 50 % of various thermal load demands. However, the independent MH storage system is difficult to effectively match the heat demand under different operating conditions, such as the complex temperature fluctuations between day and night. Kumar et al.

[29] compared the integration of four types of MH tanks into renewable energy microgrid systems and developed different thermal management strategies, highlighting the storage density advantage of solid-state hydrogen storage. In another study, Alqahtani et al. [30] combined PCM and MH to develop an energy storage system for concentrated solar power plants. However, their focus was primarily on heat storage, without addressing the comprehensive process of solar hydrogen production and storage. The summary of above literatures is shown in Table 1.

To summarize, previous studies predominantly relied on gaseous hydrogen storage in PV hydrogen production systems, and fewer considered the issue of novel hydrogen storage methods, leading to inherent constraints concerning hydrogen storage volume and compression energy consumption. Additionally, some PV hydrogen production systems employed single solid-state hydrogen storage methods while neglecting energy consumption concerns related to thermal management. Given the growing demand for hydrogen energy storage in PV systems, it is imperative to investigate the integration of MH-PCM tanks and assess their compatibility with PV systems. Nonetheless, the role of natural convection in MH-PCM tanks has been largely underestimated, despite its significant impact on the performance of hydrogen storage tanks.

Building upon the aforementioned analysis, this study firstly developed a vertical MH-PCM tank model to investigate the influence mechanism of natural convection on key system performance parameters. Subsequently, under the natural convection effect, this study analyzed the sensitivity of the thermal conductivity of PCM and hydrogen inlet pressure on performance parameters, thereby laying a precise foundation for the structural optimization of such hydrogen storage systems. Based on this MH-PCM model, this study presented a novel solid-gas coupling hydrogen storage model that combines the proposed MH-PCM solid hydrogen storage with gaseous hydrogen storage, and integrates it into the PV system. The performance parameters of this solid-gas coupling hydrogen storage were thoroughly investigated, and several optimization suggestions were provided. Additionally, this study compared this proposed hydrogen storage method with other storage methods considering storage pressure, storage volume, and energy consumption. The innovation contributions of this study can be summarized as follows.

- (1) Analysis of the impact of natural convection on hydrogen storage performance within the proposed vertical MH-PCM tank, providing insights into the heat transfer mechanism considering

**Fig. 1.** PV hydrogen production system and solid-gas coupling hydrogen storage system based on MH-PCM pack.

the natural convection effect and offering a theoretical basis for designing more efficient and stable hydrogen storage systems.

- (2) Introduction of a novel solid–gas coupling hydrogen storage method for PV hydrogen production systems. This approach can comprehensively improve storage capacity, storage volume, and energy consumption, addressing the limitations of traditional gaseous hydrogen storage methods and providing more efficient and sustainable solutions for renewable energy systems.
- (3) Quantitative evaluation of the comprehensive performance differences between solid–gas coupled hydrogen storage and other hydrogen storage methods, highlighting the potential advantages and suitable applications of solid–gas coupled hydrogen storage.

This study could provide valuable theoretical and engineering guidance for the practical implementation of such distributed hydrogen production and storage systems, aiding in the selection and decision-making for future clean energy storage technologies.

## 2. System description and model construction

### 2.1. System description

Fig. 1 depicts the PV hydrogen production and solid–gas coupling hydrogen storage systems based on the MH-PCM pack. As shown, electricity generated by the PV generator is utilized in the electrolyzer to produce hydrogen, which is then compressed to the required pressure and stored within the solid–gas coupling hydrogen storage system through the hydrogen buffer tank. The storage system comprises the MH-PCM pack and the gaseous storage tank. To meet the hydrogen storage capacity requirement of the system, the MH-PCM pack consists of 800 interconnected MH-PCM tanks. As depicted in Fig. 1, each MH-PCM tank comprises the MH, PCM, and hydrogen inlet pipe domains. LaNi<sub>5</sub> and paraffin RT35 are selected as the MH alloy and PCM, respectively, based on their material characteristics. The model used in this study is a two-dimensional center-symmetric representation of the MH-PCM tank, and the tank dimensions refer to the experimental setting parameters reported in the literature [31]. The tank has a cylindrical shape measuring 96 mm in diameter and 75 mm in height. The diameter and height of the MH domain are 50 mm and 60 mm, respectively, and the diameter and height of the hydrogen inlet pipe domain are 5 mm and 10 mm, respectively.

This study used MATLAB and Fluent computing platforms for numerical and system simulation. To enable seamless data exchange between the two platforms, real-time data storage and retrieval were achieved using 'UDF (user-defined function)' in Fluent and the 'Mex file' in MATLAB. To ensure simulation calculations without affecting the change regulations and main conclusions of the system, this study adopted similar assumptions to those in previous studies [15,22,32,33].

- (1) Local thermal equilibrium in MH-PCM tank is valid [15,22,32].
- (2) The thermophysical parameters (density, specific heat, thermal conductivity, etc.) in the MH domain remain constant [15,22,32].
- (3) Ignore the volume expansion caused by phase transformation [15,22,32].
- (4) Ignore pipeline pressure loss, radiation heat transfer and heat loss of the MH-PCM pack to the environment [15,22,32].
- (5) The electrolyzer is equipped with effective thermal management, enabling it to maintain a constant working temperature of 80°C [33].

### 2.2. Model construction

This section establishes the models for MH-PCM hydrogen storage, PV generator, electrolyzer and compressed hydrogen storage to facilitate system integration and conduct simulations for performance optimization.

#### 2.2.1. Metal hydride model

##### Mass equation.

MH hydrogen storage model includes the conservation equation of mass, momentum and energy, and the reaction kinetics equation, equilibrium pressure equation and state equation. The continuity equation and ideal gas equation of gaseous hydrogen in the MH-PCM tank, according to the law of conservation of mass [34],

$$\varepsilon \frac{\partial \rho_{H_2}}{\partial t} + \nabla \cdot (\rho_{H_2} \vec{v}) = -\dot{m}_{H_2} \quad (1)$$

$$P_{H_2} = \rho_{H_2} R_{H_2} T_{MH} \quad (2)$$

where,  $\varepsilon$  is the porosity of MH,  $\rho_{H_2}$  is the density of hydrogen, kg/m<sup>3</sup>,  $\vec{v}$  is Darcy's velocity, and the calculation can be expressed in eq. (3) [21].  $\dot{m}_{H_2}$  is the mass flow of hydrogen per unit volume, kg/s/m<sup>3</sup>,  $T_{MH}$  is the temperature in MH domain, K,  $P_{H_2}$  is the pressure of hydrogen, Pa,  $R_{H_2}$  is the gas constant of hydrogen, J/kg/K.

##### Momentum equation.

The  $\vec{v}$  is obtained from Darcy's law [35] and calculated by,

$$\vec{v} = -\frac{\kappa}{\mu} \nabla P \quad (3)$$

where,  $\kappa$  is the permeability, m<sup>2</sup>,  $\mu$  is the dynamic viscosity, Pa-s,  $\nabla P$  is the pressure gradient, Pa/m.

Similarly, the mass conservation equation for the solid material in MH domain is written as [34],

$$(1 - \varepsilon) \frac{\partial \rho_{MH}}{\partial t} = \dot{m}_{MH} \quad (4)$$

where,  $\dot{m}_{MH}$  is the mass change rate of MH per unit volume, kg/s/m<sup>3</sup>,  $\rho_{MH}$  is the density of MH, kg/m<sup>3</sup>. The density of solid MH material increases during absorption and decreases during desorption. The mass source term relationship between solid MH material and gaseous hydrogen can be written as  $\dot{m}_{MH} = -\dot{m}_{H_2}$ .

##### Energy equation.

The energy conservation equation of the MH in two-dimensional cylindrical coordinates system is expressed as [34,36],

$$(\rho C_p)_{\text{eff}} \frac{\partial T}{\partial t} + \rho_{H_2} C_{p,H_2} \vec{v} \cdot \nabla T = \nabla \cdot (k_{\text{eff,MH}} \nabla T) - \dot{m}_{H_2} [\Delta H + T_{MH} (C_{p,H_2} - C_{p,MH})] \quad (5)$$

$$(\rho C_p)_{\text{eff}} = [\varepsilon \rho_{H_2} C_{p,H_2} + (1 - \varepsilon) \rho_{MH} C_{p,MH}] \quad (6)$$

$$k_{\text{eff,MH}} = \varepsilon k_{H_2} + (1 - \varepsilon) k_{MH} \quad (7)$$

where,  $(\rho C_p)_{\text{eff}}$  is the effective volume average specific heat of hydrogen and MH, J/m<sup>3</sup>/K,  $k_{\text{eff,MH}}$ ,  $k_{H_2}$  and  $k_{MH}$  are the effective thermal conductivity, the thermal conductivity of hydrogen and the thermal conductivity of MH, W/m/K.  $\Delta H$  is the reaction enthalpy, J/kg.  $C_{p,H_2}$  and  $C_{p,MH}$  are the specific heat of hydrogen and MH, respectively, J/kg/K.

##### Kinetic reaction.

In the adsorption process, the hydrogen pressure in the tank is lower than the pressure equilibrium pressure. The adsorbing rate is relative to the reaction kinetics of MH and the equilibrium pressure, can be calculated as [35],

$$\dot{m}_{\text{abs}} = -C_{\text{abs}} \exp\left(-\frac{E_{\text{abs}}}{RT_{MH}}\right) \ln\left(\frac{P_{H_2}}{P_{\text{eq}}}\right) (\rho_{MH,\text{sat}} - \rho_{MH}) \quad (8)$$

where,  $C_{\text{abs}}$  is the hydrogen adsorption constant, s<sup>-1</sup>,  $E_{\text{abs}}$  is the activation energy of the adsorption reaction, J/mol,  $\rho_{MH,\text{sat}}$  and  $\rho_{MH,\text{emp}}$  are the saturated density and the hydrogen-free density of the MH, respectively, kg/m<sup>3</sup>.

The equilibrium pressure during the adsorption process according to



**Table 2**

Main parameters for numerical simulation of MH-PCM tank.

Symbol	Parameters	Value
$R$	Universal gas constant, J/mol/K	8.314
$k_{MH}$	Thermal conductivity of MH, W/m/K	2
$k_{H2}$	Thermal conductivity of hydrogen, W/m/K	0.1815
$C_{p,H2}$	Specific heat of hydrogen, J/kg/K	14,890
$C_{p,MH}$	Specific heat of the MH, J/kg/K	419
$C_{abs}$	Absorption constant of MH, $s^{-1}$	9.571
$E_{abs}$	Activation energy, J/mol	16,473
$\Delta H$	Enthalpy of reaction, J/kg	$1.539 \times 10^7$
$U$	Convective heat transfer coefficient, W/m <sup>2</sup> /K	1652
$\kappa$	Permeability, m <sup>2</sup>	$10^{-8}$
$\mu$	Dynamic viscosity, Pa·s	$8.4 \times 10^{-6}$
$\varepsilon$	Porosity of metal hydride	0.5
$\rho_{MH,emp}$	Empty density of the MH, kg/m <sup>3</sup>	7164
$\rho_{MH,sat}$	Saturated density of the MH, kg/m <sup>3</sup>	7259
$\rho_{PCM}$	Density of PCM (Solid/Liquid), kg/m <sup>3</sup>	880/760
$T_m$	Melting/Solidification temperature, K	316.15/317.15
$C_{p,PCM}$	Specific heat of PCM (Solid/Liquid), J/kg/K	1800/2400
$k_{PCM}$	Thermal conductivity of PCM, W/m/K	0.2
$L$	Latent heat of PCM, J/kg	157,000

van't Hoff equation can be expressed as [35],

$$\ln \frac{P_{eq}}{P_{atm}} = A_{abs} - \frac{B_{abs}}{T} \quad (9)$$

where, the values of the plateau pressure coefficients  $A_{abs}$  and  $B_{abs}$  for absorption can be determined from the literature [35],  $A_{abs} = 10.57$ ,  $B_{abs} = 3704.6$ .

### 2.2.2. Phase change material model

PCM can be used to store the heat energy released by the MH adsorption process, and the energy conservation equation for PCM heat storage can be expressed as the total volume enthalpy and temperature of constant thermophysical properties [37],

$$\frac{\partial H}{\partial t} = \nabla \cdot (k_{PCM} \nabla T) \quad (10)$$

where,  $k_{PCM}$  is the thermal conductivity of PCM, W/m/K,  $H$  is the total volume enthalpy of PCM, J/kg, and can be expressed as the sum of sensible and latent enthalpy [38],

$$H(T) = h(T) + \rho_{PCM} L f(T) \quad (11)$$

where,  $f$  is the liquid mass fraction of PCM,  $L$  is the latent heat of PCM, J/kg,  $h$  is the sensible enthalpy, J/kg, and can be expressed as [38],

$$h(T) = \int_{T_m}^T \rho_{PCM} C_{p,PCM} dT \quad (12)$$

where,  $\rho_{PCM}$  is the density of PCM, kg/m<sup>3</sup>,  $C_{p,PCM}$  is the specific heat, J/kg/K,  $T_m$  represents the melting temperature, T.

The two-dimensional heat transfer equation in the PCM domain can be expressed as [37],

$$\rho_{PCM} C_{p,PCM} \frac{\partial T}{\partial t} = \nabla \cdot (k_{PCM} \nabla T) - \rho_{PCM} L \frac{\partial f}{\partial t} \quad (13)$$

In this study, paraffin RT35 undergoes a phase transition from solid to liquid, resulting in a density change from 880 kg/m<sup>3</sup> to approximately 760 kg/m<sup>3</sup>. This transition absorbs heat, causing the temperature to shift from 316.15 K to 317.15 K, and the specific heat to change from 1800 J/kg/K to 2400 J/kg/K.

The main parameters for numerical simulation in this study are shown in Table 2 [31,34,35].

### 2.2.3. Photovoltaic generator model

This section presents a comprehensive PV model that incorporates the widely acknowledged classical current-voltage characteristic model.

**Table 3**

Main parameters of PV generator [39].

Symbol	Parameters	Value
$I_{sc}$	Short-circuit current, A	8.21
$V_{oc}$	Open-circuit voltage, V	32.9
$N_p$	Parallel number of PV panels	27
$N_s$	Series of PV panels	10
$q$	Electronic charge, C	$1.6 \times 10^{-19}$
$a$	Ideal parameter of the diode	1.4284
$b$	Boltzmann constant, J/K	$1.38 \times 10^{-23}$
$N$	Number of PV cells in each PV panel	54

This model considers the relationships between primary factors such as irradiance, temperature, and current. The current-voltage electrical characteristics of the PV generator can be expressed as [39],

$$I_{pv} = I_{ph} - I_0 \left[ \exp \left( \frac{V_{pv} + 0.221 I_{pv} N_s / N_p}{N_s a N b T / q} \right) - 1 \right] \quad (14)$$

where,  $I_{ph}$  and  $I_0$  are the photogenerated current due to the movement of these free electrons and reverse saturated leakage current flowing through the diode, respectively.  $I_{pv}$  is the operation current, A.  $V_{pv}$  is the operating voltage, V.  $N_p$  and  $N_s$  are the parallel and series number of PV panels respectively.  $N$  is the number of PV cells in each PV panel.  $a$  is the ideal parameter of the diode,  $q$  is the electronic charge,  $b$  is Boltzmann constant,  $T$  is the operation temperature, K.

The calculations of  $I_{ph}$  and  $I_0$  can be expressed as [39],

$$I_{ph} = \frac{G}{1000} [I_{sc} N_p + 0.0038 N_p (T - T_{atm})] \quad (15)$$

$$I_0 = \frac{[I_{sc} N_p + 0.0038 N_p (T - T_{atm})]}{\exp(V_{oc} q / a N b T) - 1} \quad (16)$$

where,  $G$  is the irradiance intensity, W/m<sup>2</sup>,  $I_{sc}$  is the short-circuit current of each PV panel, A,  $V_{oc}$  is the open-circuit voltage of each PV panel, V.  $T_{atm}$  is the atmosphere temperature, 298.15 K.

The power generated by the PV generator can be expressed as [39],

$$Pow_{pv} = I_{pv} V_{pv} \quad (17)$$

PV generator is intricately related to irradiance conditions and temperature, and this simplified model can capture the dynamic relationship between power generation and these environmental factors. This model serves as a crucial foundation for our research, enabling us to explore the dynamic interplay between the PV generator, hydrogen production, and novel storage systems. The main parameters used for PV generator simulation in this study are mainly from the literature [39], as shown in Table 3.

### 2.2.4. Electrolyzer model

The electrolyzer model employed in this study simulates a KOH alkaline electrolyzer due to its high stability and energy conversion efficiency in PV systems. This model establishes the relationship between the cell voltage and various contributing factors, including the reversible voltage, ohmic voltage, and concentration polarization voltage, which can be written as [8,33],

$$v_{el} = \frac{\Delta G_f}{2F} + \frac{r_1 + r_2 T}{A_{cell}} I_{el} + (s_1 + s_2 T + s_3 T^2) \log \left( \frac{t_1 + t_2 T + t_3 T^2}{A_{cell}} I_{el} + 1 \right) \quad (18)$$

where,  $\Delta G_f$  is the Gibbs free energy change, J,  $F$  is Faraday constant, 96,485C/mol, the reversible cell voltage is taken as 1.229 V.  $T$  is the operation temperature, K,  $I_{el}$  is the operation current, A,  $A_{cell}$  is the area of the electrodes, m<sup>2</sup>,  $r_1$  and  $r_2$  are ohmic resistances of electrolyte,  $s_1$ ,  $s_2$ ,  $s_3$ ,  $t_1$ ,  $t_2$ ,  $t_3$  and  $t_4$  are parameters for overvoltage on electrodes.

For the electrolyzer with  $N_{cell}$  cells in series, the output voltage of the

**Table 4**  
main parameters of the electrolyzer [33].

Symbol	Parameters	Value
$A_{\text{cell}}$	Area of the electrodes, $\text{m}^2$	0.25
$N_{\text{cell}}$	Number of electrolyzer cells	80
$r_1$	Parameters of electrolyte, $\Omega \cdot \text{m}^2$	$7.33 \times 10^{-5}$
$r_2$	Parameters of electrolyte, $\Omega \cdot \text{m}^2/\text{K}$	$-1.11 \times 10^{-47}$
$s_1$	Parameters of electrolyte, V	0.159
$s_2$	Parameters of electrolyte, V/K	0.00138
$s_3$	Parameters of electrolyte, V/K <sup>2</sup>	$-1.61 \times 10^{-5}$
$t_1$	Parameters of electrolyte, $\text{m}^2/\text{A}$	0.016
$t_2$	Parameters of electrolyte, $\text{m}^2/\text{K}/\text{A}$	-1.302
$t_3$	Parameters of electrolyte, $\text{m}^2/\text{K}^2/\text{A}$	421

electrolyzer can be calculated as [8,33],

$$V_{\text{el}} = N_{\text{cell}} V_{\text{el}} \quad (19)$$

According to Faraday's law, the ideal hydrogen production rate can be calculated. However, because of the parasitic current, the actual hydrogen production rate is generally less than the theoretical hydrogen production rate [8,33],

$$\dot{n}_{\text{el, H}_2} = \eta_{\text{el}} \frac{N_{\text{el}} I_{\text{el}}}{2F} \quad (20)$$

where,  $\dot{n}_{\text{el, H}_2}$  presents the hydrogen production mole rate, mol/s,  $\eta_{\text{el}}$  is the Faraday efficiency, 0.9.

This electrolyzer model can provide the necessary foundation for simulating and analyzing hydrogen production performance under varying operational conditions. Table 4 shows the main parameters of the electrolyzer.

#### 2.2.5. Compressed hydrogen storage model

Hydrogen generated by the PV generator typically requires compression and cooling to attain the required storage pressure and temperature, resulting in parasitic energy consumption. Given the low-pressure characteristics of the proposed solid-gas coupling hydrogen storage, this study primarily focuses on evaluating energy loss caused by compression. The power consumed by the compressor under ideal adiabatic conditions can be expressed as [40],

$$P_{\text{ow,com}} = \frac{C_{p,\text{H}_2} T_{\text{com}}}{\eta_{\text{com}}} \left[ \left( \frac{P_{\text{H}_2}}{P_0} \right)^{\frac{\gamma-1}{\gamma}} - 1 \right] W_{\text{com}} \quad (21)$$

where,  $T_{\text{com}}$  is the inlet temperature of the compressor, K,  $\gamma$  is the adiabatic index, 1.4.  $\eta_{\text{com}}$  is the compressor efficiency, 0.95,  $W_{\text{com}}$  is the flow at the outlet of the compressor, kg/s.  $P_0$  and  $P_{\text{H}_2}$  is the gas pressure before and after compression, respectively, Pa.

However, when the hydrogen pressure exceeds 100 bar, the deviation degree of the hydrogen compression process from the ideal gas adiabatic compression process becomes more pronounced. To account for this non-ideal state of hydrogen, a compression coefficient  $Z$  is introduced to compensate for the non-ideal state of hydrogen, and  $Z$  depends on the pressure and temperature of hydrogen, which can be expressed as [7,41],

$$P_{\text{H}_2} \text{Vol}_{\text{H}_2} = ZnRT_{\text{H}_2} \quad (22)$$

$$Z = 1 + k_Z \left( \frac{P_{\text{H}_2}}{P_{\text{atm}}} \right) \quad (23)$$

where,  $\text{Vol}_{\text{H}_2}$  is the hydrogen volume,  $\text{m}^3$ ,  $k_Z$  is the empirical constant, taken as 0.000631,  $P_{\text{atm}}$  is the standard atmospheric pressure, Pa, and the more detailed expressions and detailed parameters are given in the literature [40,41].

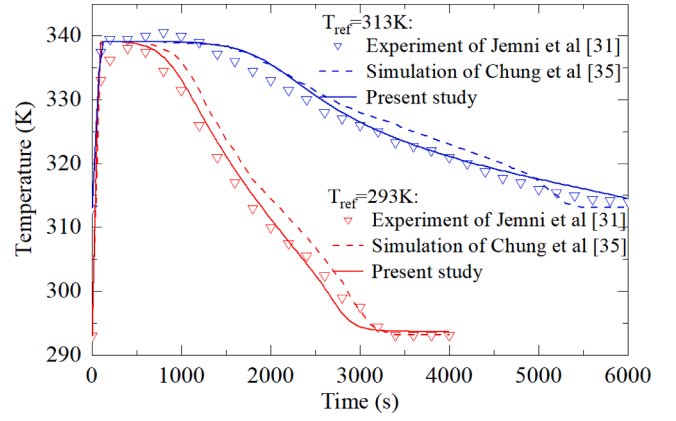


**Fig. 2.** Comparisons of the present simulation results and the results in the literature [31] and literature [35].

#### 2.3. Model validation

##### 2.3.1. Boundary conditions of the MH-PCM model

The simulation results for the MH model are rigorously validated by comparing them with both experimental data from the literature [31] and the simulation results in the literature [35] due to the mass and energy source terms. The specific conditions for this validation are as follows: when the initial temperature is 293 K, the inlet pressure rises linearly from the initial pressure of 0.143 MPa (corresponding to the initial equilibrium temperature of 293 K) to 0.8 MPa within 100 s, and then remains constant until the end of the simulation. When the initial temperature is 313 K, the inlet pressure rises linearly from the initial pressure of 0.321 MPa (corresponding to the initial equilibrium temperature of 313 K) to 0.8 MPa within 100 s, maintained at this level until the end of the simulation.

When  $z = l_{\text{in}}$ , for the condition that the initial temperature is 293 K,

$$T(r, l_{\text{in}}, t) = T_0 = 293\text{K} \quad (24)$$

$$P(r, l_{\text{in}}, t) = P_0 = 0.143\text{MPa} \quad (25)$$

$$P(r, l_{\text{in}}, t) = P_{100\text{s}} = 0.8\text{MPa} \quad (26)$$

For the condition that the initial temperature is 313 K,

$$T(r, l_{\text{in}}, t) = T_0 = 313\text{K} \quad (27)$$

$$P(r, l_{\text{in}}, t) = P_0 = 0.321\text{MPa} \quad (28)$$

$$P(r, l_{\text{in}}, t) = P_{100\text{s}} = 0.8\text{MPa} \quad (29)$$

On the  $z$ -axis ( $r = 0$ ), the computational domain is centrosymmetric,

$$\frac{\partial T}{\partial r}(0, z, t) = 0 \quad (30)$$

The heat flow through each part of the tank can be expressed as follows,

When  $r = r_{\text{wall}}$ ,

$$\frac{\partial T}{\partial r}(r_{\text{wall}}, z, t) = 0 \quad (31)$$

When  $z = 0$ ,

$$\frac{\partial T}{\partial z}(r, 0, t) = 0 \quad (32)$$

When  $z = l_{\text{wall}}$ ,

$$\frac{\partial T}{\partial z}(r, l_{\text{wall}}, t) = 0 \quad (33)$$

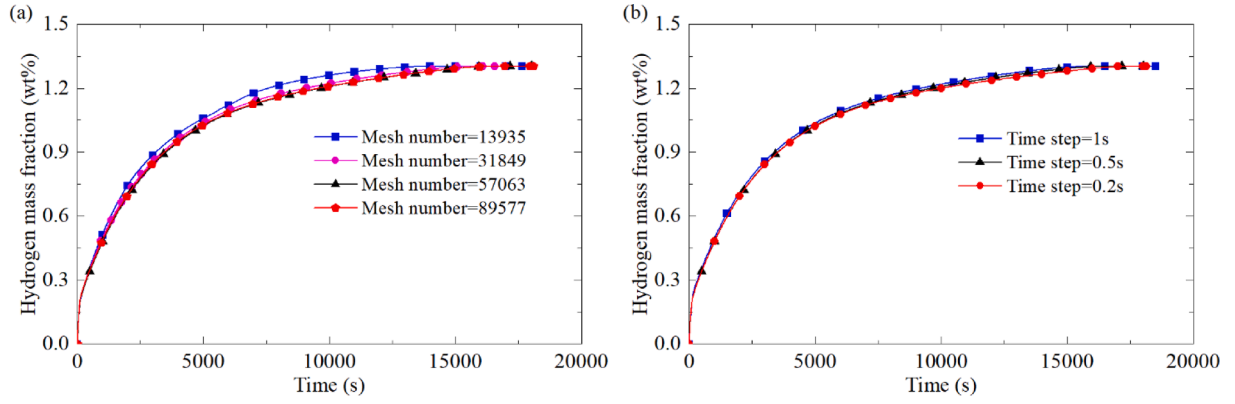


**Fig. 3.** Change curves of hydrogen mass fraction under different grid numbers and simulation steps (a) grid independence verification (b) simulation step independence verification.

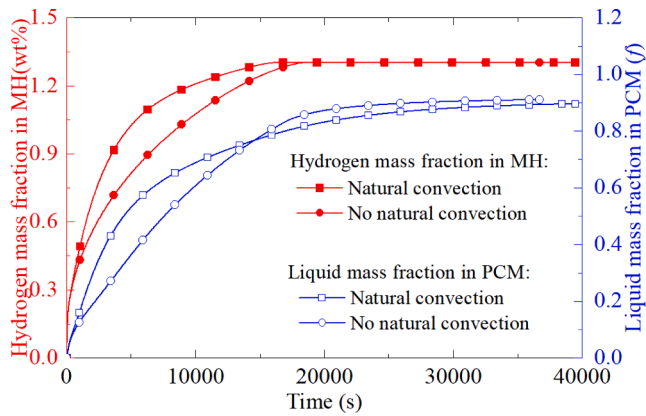


**Fig. 4.** The change rules of hydrogen mass fraction in MH and liquid mass fraction in PCM with natural convection.

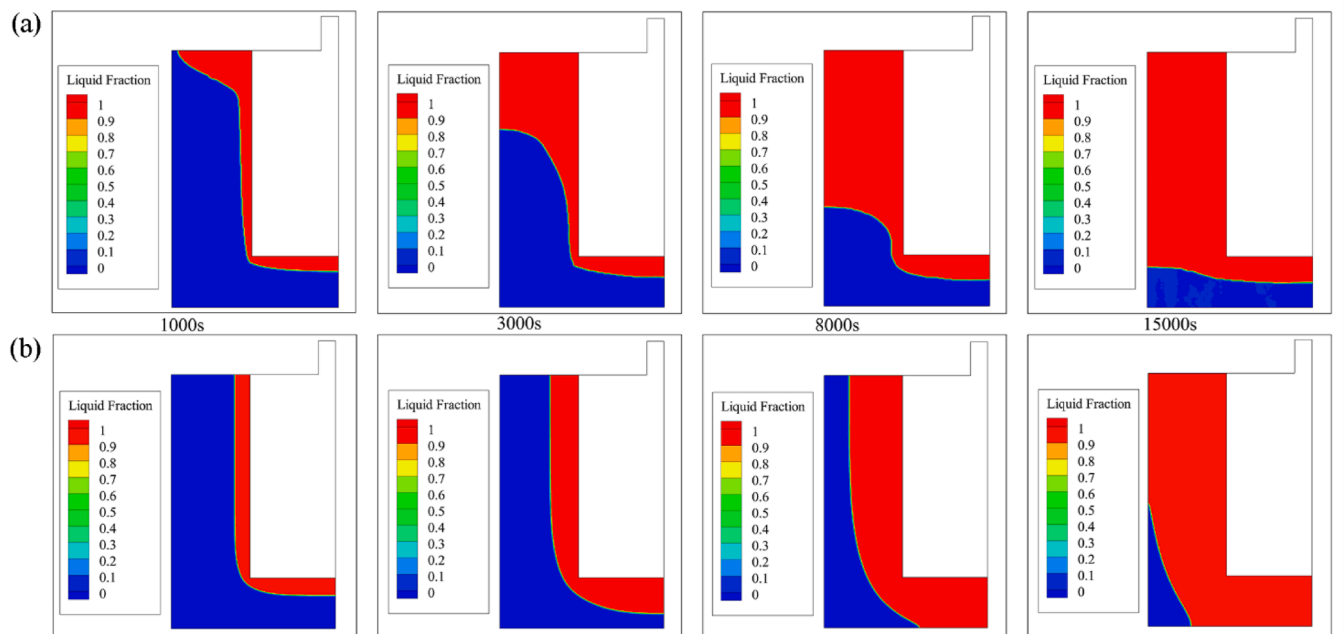
### 2.3.2. Validation results

Fig. 2 illustrates comparisons of the temperature curve at the coordinates  $r = 15$  mm and  $z = 35$  mm of the MH-PCM tank. This study demonstrates that the maximum error between the obtained simulation results and those reported in the literature is less than 5 %, which confirms the model appropriateness for further simulation investigations.

Additionally, the MH-PCM model is verified for grid independence and step independence using grid numbers 13935, 31849, 57,063 and 89577, and step lengths of 0.2 s, 0.5 s and 1 s, respectively. As depicted in Fig. 3, The verification results reveal that the maximum error in the hydrogen mass fraction is less than 1 % when the grid number exceeds 57,063 or the simulation step less than 0.5 s. Considering the computational complexity and model accuracy, this study selected the grid number 57,063 and the simulation step 0.5 s.

## 3. Performance analysis of MH-PCM hydrogen storage

This section mainly analyzes the influence of natural convection and key parameters on the hydrogen storage performance of the MH-PCM tank, laying the foundation for the integrated PV hydrogen production



**Fig. 5.** Change process of PCM liquid mass fraction at different times (a) Natural convection (b) No natural convection.

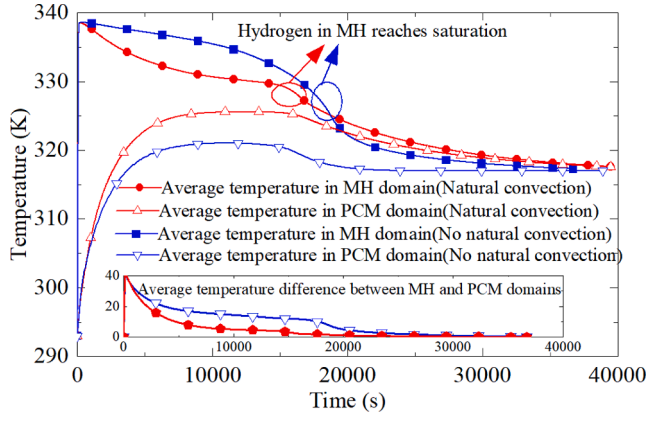


Fig. 6. Variation curves of average temperature in MH and PCM domains under considering (red line) and not considering (blue line) natural convection.

system.

### 3.1. Influence of natural convection

This section investigates the influence of natural convection on the hydrogen mass fraction, PCM liquid mass fraction, and temperature of the MH and PCM domains, aiming to explore an effective approach to suppress the effects of natural convection.

#### 3.1.1. Variations in hydrogen mass fraction and PCM liquid mass fraction

Fig. 4 depicts the variations in hydrogen mass fraction in MH and liquid mass fraction in PCM under natural convection. Fig. 5 shows the corresponding PCM liquid mass fraction changes at different intervals. The results indicate that natural convection can enhance the hydrogen storage rate, particularly during the mid-phase of the hydrogen storage process. Notably, the MH-PCM tank exhibits an average hydrogen storage rate approximately 12.7 % higher when natural convection is considered, as opposed to when it was neglected.

During the initial stage of the hydrogen storage process, the released heat primarily transforms into sensible heat within the PCM, and the impact of natural convection on the hydrogen storage rate remains minimal. However, as the reaction progresses, the released heat predominantly becomes latent heat within the PCM, leading to its melting and initiating natural convection, which enhances heat transfer and improves the hydrogen storage rate. In the later stage of the process, as solid-liquid separation within the PCM becomes apparent, the impact of natural convection on heat transfer diminishes. During this stage, the melting and hydrogen storage rates are chiefly influenced by the PCM thermal conductivity.

To sum up, this section underscores the substantial influence of natural convection and heat conduction on the hydrogen storage rate within the MH-PCM tank. Natural convection takes precedence during the intermediate stage of hydrogen storage, whereas heat conduction plays a more prominent role in the initial and later stages. To enhance the overall hydrogen storage rate of such MH-PCM tanks, it is recommended to strengthen the heat transfer mechanisms at the bottom of the tank, thereby improving hydrogen storage efficiency throughout the entire process.

#### 3.1.2. Variations in the temperature of MH and PCM domains

Fig. 6 depicts the variation curves of the average temperature in MH and PCM domains under considering and not considering natural convection. Whether natural convection is considered or not, in the initial stage of the hydrogen storage process, the average temperature within the MH domain rises to approximately 338.3°C as the hydrogen inlet pressure reaches 8 bar. Subsequently, it gradually decreases as heat is transferred to the PCM domain. In the middle of the hydrogen storage

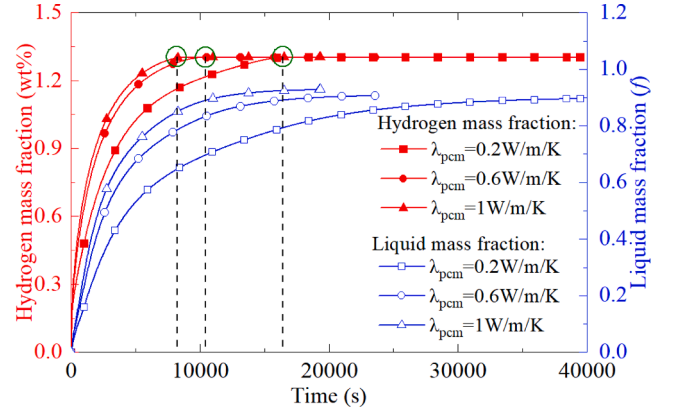


Fig. 7. Influence of PCM thermal conductivity on hydrogen mass fraction and PCM liquid mass fraction.

process, the average temperature within the MH domain has a significant decline, which can be attributed to the hydrogen storage capacity approaching saturation and the depletion of heat source.

When considering the natural convection, the average temperature in MH domain is higher than that without considering the natural convection, while the average temperature in PCM domain is lower. To evaluate the overall heat transfer effectiveness, Fig. 6 also illustrates the curve of the average temperature difference between the MH and PCM domains. Considering the natural convection effect, the average temperature difference remains relatively low, indirectly indicating that natural convection enhances the heat transfer effect between the MH and PCM domains. However, as the hydrogen storage capacity approaches saturation, the average temperature difference gradually decreases. These findings reaffirm that the natural convection effect weakens in the later stage of the hydrogen storage process, while the impact of heat conduction becomes more pronounced.

### 3.2. Sensitivity analysis of main parameters

This section conducts a sensitivity analysis to investigate the impact of PCM thermal conductivity and hydrogen inlet pressure on the performance parameters, considering the effects of natural convection. The objective is to identify the key factors significantly influencing hydrogen storage performance parameters and provide optimization recommendations.

#### 3.2.1. PCM thermal conductivity

Fig. 7 presents the influence of PCM thermal conductivity on the hydrogen mass fraction and PCM liquid mass fraction. As PCM thermal conductivity increases from 0.2 W/m/K to 0.6 W/m/K and 1 W/m/K, the hydrogen storage rate gradually improves, with corresponding hydrogen storage times of 16795 s, 10419 s and 8898 s, respectively. Compared to PCM thermal conductivity of 0.2 W/m/K, the hydrogen storage time decreases by approximately 40.0 % and 47.0 % when the PCM thermal conductivity is 0.6 W/m/K and 1 W/m/K, respectively. Nevertheless, the rate of improvement gradually diminishes because the primary limiting factor for the hydrogen storage process shifts from PCM thermal conductivity to the temperature difference driving heat transfer.

Hence, properly enhancing the PCM thermal conductivity can effectively improve the hydrogen storage rate, particularly when initially low. Additionally, using a PCM with a lower phase change temperature can increase the temperature difference for heat transfer, thereby improving the hydrogen storage rate. Meanwhile, it's essential to ensure that the temperature requirements for hydrogen desorption are met at a minimum.



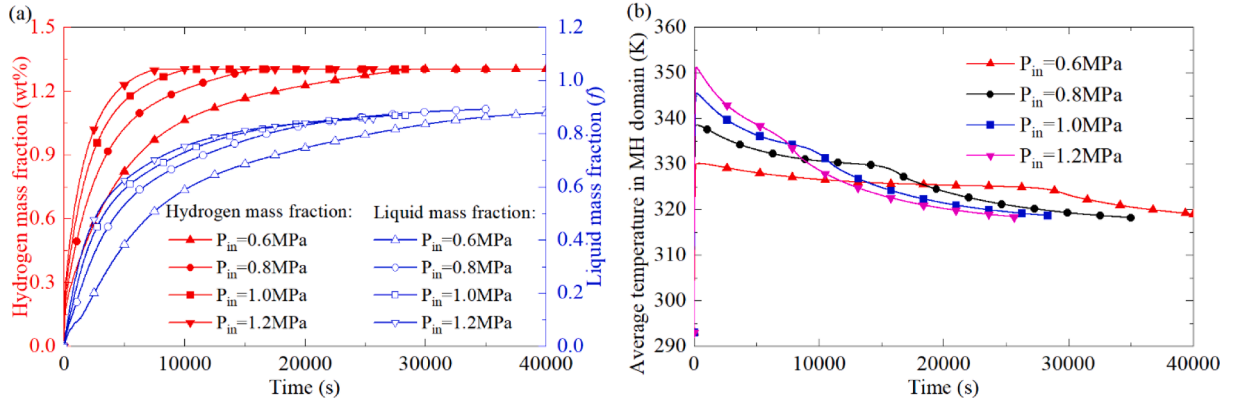


Fig. 8. Influence of hydrogen inlet pressure on the performance parameters of MH-PCM tank (a) Hydrogen mass fraction and PCM liquid mass fraction (b) Average temperature of MH domain.

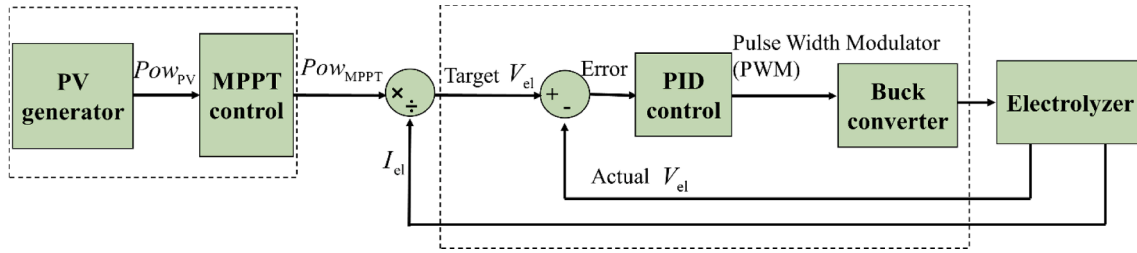


Fig. 9. The control block diagram of the photovoltaic hydrogen generation system.

### 3.2.2. Hydrogen inlet pressure

Fig. 8 depicts the influence of hydrogen inlet pressure on the performance parameters of the MH-PCM tank. In Fig. 8 (a), both the hydrogen storage rate and PCM melting rate gradually increase with rising hydrogen inlet pressure from 0.6 MPa, 0.8 MPa, 1 MPa and 1.2 MPa, with corresponding hydrogen storage times of 30125 s, 16795 s, 10950 s and 8150 s, respectively. Compared to the hydrogen inlet pressure of 0.6 MPa, the hydrogen storage time decreases by around 44.2 %, 63.7 % and 72.9 % when the hydrogen inlet pressure is 0.8 MPa, 1 MPa and 1.2 MPa, respectively.

Fig. 8(b) shows that, with increased hydrogen inlet pressure, the initial average temperature in the MH domain rises, and the temperature decrease rate also increases. This indicates an improved heat dissipation effect of MH under high hydrogen inlet pressure. However, higher hydrogen inlet pressure results in increased compression power consumption. Therefore, for comprehensive consideration, it is recommended that the hydrogen inlet pressure of such storage tanks be set at around 1 MPa.

## 4. Analysis of PV hydrogen production and storage system

This section presents a comprehensive analysis of the PV hydrogen production and storage system, focusing on integrating a solid-gas coupling hydrogen storage system based on the MH-PCM pack. The objective is to assess the storage performance over 8 h on a typical day and compare various hydrogen storage modes to provide optimization recommendations.

### 4.1. PV hydrogen production control strategy

To optimize hydrogen production, the maximum power point tracking (MPPT) method is employed. This technique could dynamically adjust the output of PV generator to maximize energy utilization under varying environmental conditions, and this approach is implemented using the disturbance observation method. Additionally, this study

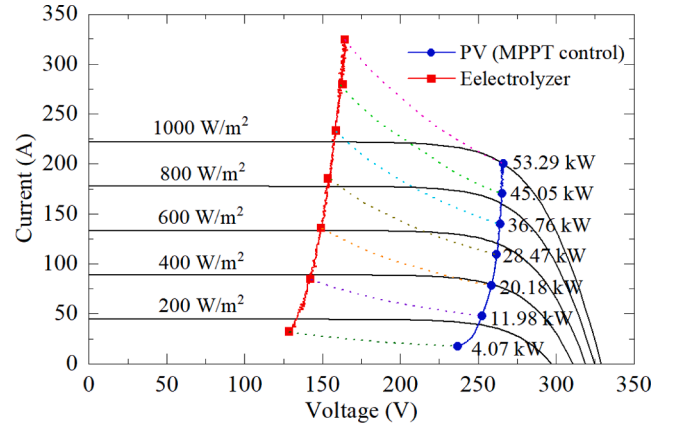
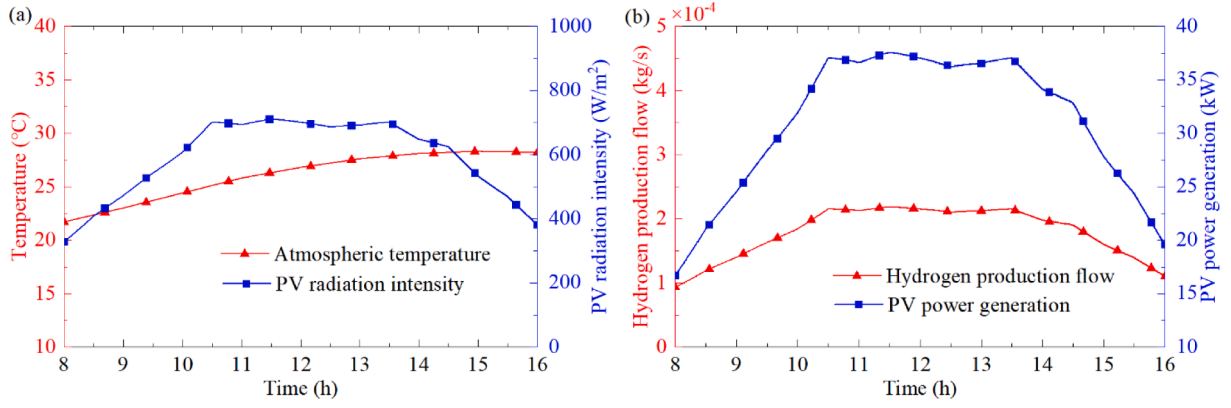


Fig. 10. Power matching curve of PV generator and electrolyzer.

adopts the indirect coupling PV hydrogen production control mode to improve the flexibility of power matching between the PV generator and electrolyzer, and ensure efficient hydrogen production. The control block diagram is illustrated in Fig. 9. Following MPPT regulation, the output voltage of the PV generator undergoes reduction through a Buck circuit to achieve precise power alignment with the electrolyzer. As shown in Fig. 10, the matching curve illustrates that power matching proves effective under the primary simulation operating conditions in this study.

Taking Jinan City, Shandong Province, China as a case study, an 8-hour simulation is selected as the time frame to reflect the change rules of hydrogen production and storage under the prevailing operating conditions. Fig. 11 (a) illustrates the curves of typical daily temperature and irradiance intensity, and Fig. 11 (b) shows the power curves of the PV generator and hydrogen production flow. Notably, there is an apparent similarity in the trends of PV generator power, hydrogen



**Fig. 11.** Curves of PV hydrogen production simulation results (a) Typical daily temperature and irradiance intensity (b) Power of PV generation and hydrogen production flow.

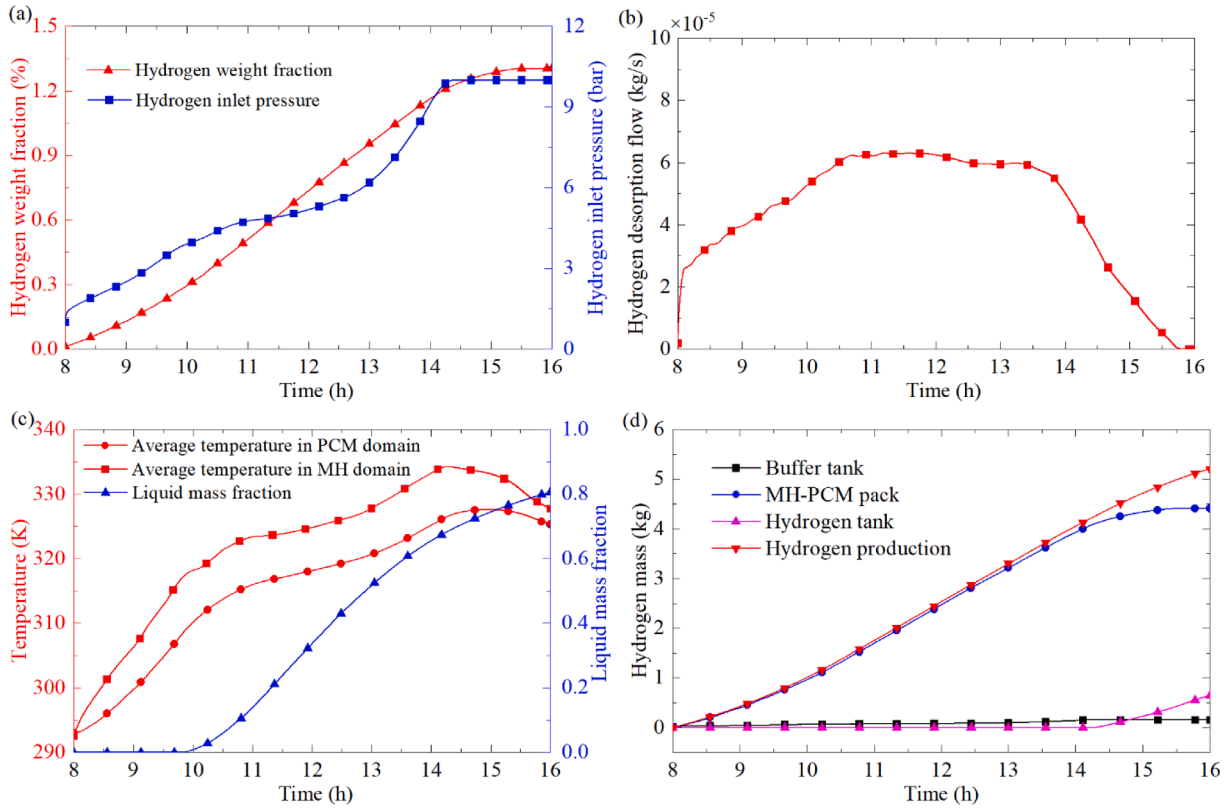


**Fig. 12.** Performance curves of the hydrogen storage system (a) Hydrogen mass fraction and hydrogen inlet pressure (b) Hydrogen storage flow (c) PCM liquid mass fraction and temperature in various domains of the MH-PCM tank (d) Mass of hydrogen production and hydrogen mass in the hydrogen buffer tank, MH-PCM tank and gaseous hydrogen storage tank.

production rate, and irradiance intensity. This indicates a strong positive correlation between hydrogen production rate and irradiance intensity.

#### 4.2. Performance analysis of hydrogen storage system

Fig. 12 (a) and (b) depict the curves of hydrogen mass fraction, inlet pressure, and hydrogen storage flow, respectively. Fig. 12 (c) depicts the curves of PCM liquid mass fraction and temperature in various domains of the MH-PCM tank. Fig. 12 (d) shows the mass curves of hydrogen production and hydrogen in the hydrogen buffer tank, MH-PCM tank and gaseous hydrogen storage tank. According to the various characteristics of hydrogen mass fraction in the MH-PCM tank, this study divides the hydrogen storage process into four stages.

In the initial stage, hydrogen inlet pressure and storage flow steadily increase. During this stage, the heat absorbed by PCM primarily serves to raise the medium's temperature, resulting in minimal changes in the liquid mass fraction of the PCM.

Moving to the middle stage, the increase in hydrogen inlet pressure begins to level off as the hydrogen production flow reaches its maximum, thereby the hydrogen storage rate gradually remains stable as the hydrogen storage flow reaches approximately  $6 \times 10^{-5}$  kg/s. Besides, during this stage, the heat absorbed by PCM primarily supports the phase change reaction, resulting in a slower increase in the liquid mass fraction and a slower rise in the average temperature of each domain within the MH-PCM tank.

In the later stage, the hydrogen storage rate drops significantly due to

**Table 5**

Comparison of hydrogen storage performance of various hydrogen storage methods.

Hydrogen storage modes	Storage pressure (MPa)	Total storage volume (m <sup>3</sup> /kg)	Compression consumption (kJ/kg)	Thermal management consumption (kJ/kg)
MH storage	1.0	0.021	$0.41 \times 10^4$	$1.54 \times 10^4$
MH-PCM storage	1.0	0.096	$0.41 \times 10^4$	0
Solid-gas coupling storage based on MH-PCM pack	1.0	0.250	$0.41 \times 10^4$	0
Gaseous storage	1.0	1.209	$0.41 \times 10^4$	0
Gaseous storage	5.9	0.250	$0.97 \times 10^4$	0
Gaseous storage	35.0	0.042	$1.90 \times 10^4$	0
Gaseous storage	70.0	0.025	$2.41 \times 10^4$	0

the reduced hydrogen production flow and the approaching saturation of the hydrogen mass fraction. Consequently, the hydrogen inlet pressure rises rapidly once more, ultimately reaching the set value of 10 bar as the hydrogen storage process nears completion.

In the final stage, the hydrogen mass fraction approaches saturation, and any remaining hydrogen generated by the PV generator is stored in the gaseous hydrogen storage tank.

#### 4.3. Performance comparison of various hydrogen storage methods

Table 5 presents the performance comparison data of various hydrogen storage methods, including storage pressure, total storage volume, compression consumption, and thermal management consumption. The corresponding distribution diagram and sensitiveness are visually shown in Fig. 13. Traditional MH hydrogen storage exhibits a relatively low total storage volume but entails high thermal management energy consumption during the hydrogen absorption and desorption processes. In contrast, due to its heat storage effect, MH-PCM hydrogen storage boasts lower total energy consumption and total storage volume. Nevertheless, as previously elucidated, MH-PCM storage exhibits a slower hydrogen storage rate due to the phase transition process. Furthermore, compared to MH-PCM hydrogen storage, the solid-gas coupling hydrogen storage based on the MH-PCM pack has a larger total storage volume.

Although low-pressure gaseous hydrogen storage boasts low

compression energy consumption, it requires a large storage volume. Specifically, at an identical storage pressure of 1 MPa, the occupied volume of gaseous hydrogen storage is approximately 4.85 times greater than that of solid-gas coupling hydrogen storage based on the MH-PCM pack. Conversely, high-pressure gaseous hydrogen storage has a smaller occupied volume, but the compression energy consumption is significant. Regarding a fixed total storage volume of 1.30 m<sup>3</sup>, the compression energy consumption for gaseous storage is approximately 2.37 times higher than that of solid-gas coupling hydrogen storage based on the MH-PCM pack.

Consequently, the findings indicate that MH-PCM hydrogen storage and solid-gas coupling hydrogen storage based on the MH-PCM pack exhibit excellent comprehensive performance. Additionally, provided that the hydrogen storage system can meet the dynamic requirements of the overall design, increasing the coupling ratio of solid and gaseous storage capacity presents a viable approach to reduce the total storage volume further.

#### 5. Conclusion

This study presents a novel solid-gas coupling hydrogen storage model designed for PV hydrogen production system and evaluates its hydrogen storage performance. Firstly, a vertical MH-PCM tank model is developed to investigate the influence of natural convection, PCM thermal conductivity, and hydrogen inlet pressure on hydrogen storage performance parameters. Subsequently, a solid-gas coupling hydrogen storage model based on the MH-PCM storage is integrated into the PV hydrogen production system to analyze the comprehensive performance. Finally, the study compares the storage pressure, storage volume, and energy consumption across various hydrogen storage modes. The main conclusions are summarized as follows.

- (1) Natural convection and PCM thermal conductivity are the primary factors affecting the hydrogen storage rate of the MH-PCM tank. Natural convection predominantly impacts the middle stage of the hydrogen storage process, while heat conduction plays a more substantial role during the initial and later stages of the hydrogen storage process.
- (2) Considering natural convection leads to an approximately 12.7 % increase in the average hydrogen storage rate of the MH-PCM tank, compared to when natural convection is not considered. To improve the overall hydrogen storage efficiency of the MH-PCM tank, it is recommended to focus on structural optimization and heat transfer enhancement at the bottom of the tank.
- (3) Optimizing the PCM thermal conductivity and increasing the hydrogen inlet pressure can improve the hydrogen storage rate in the MH-PCM tank, especially when these parameters are

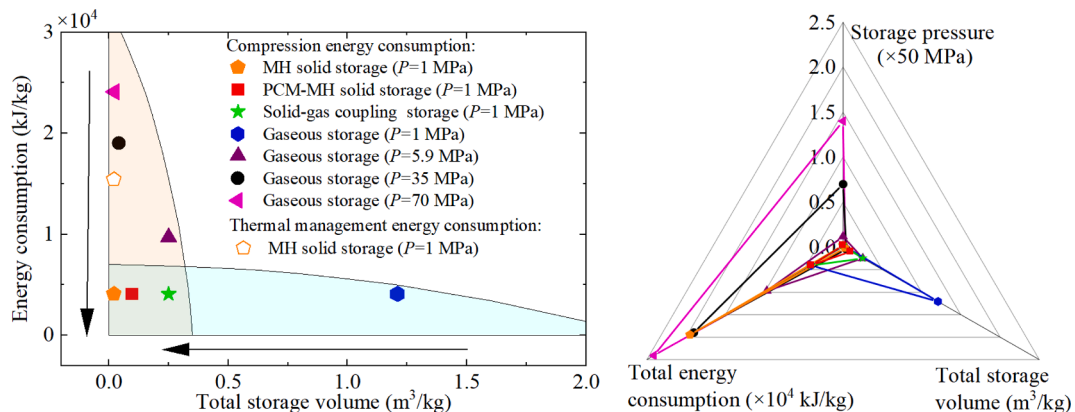


**Fig. 13.** Distribution diagram and sensitiveness for comparison of storage pressure, total storage volume, compression consumption and thermal management consumption performance of various hydrogen storage modes.

suboptimal. However, to strike a balance between compression energy consumption and hydrogen storage efficiency, it is recommended to maintain a hydrogen inlet pressure of approximately 1 MPa.

- (4) In this PV system, the solid–gas coupling hydrogen storage based on the MH-PCM pack exhibits excellent comprehensive hydrogen storage performance. Additionally, provided that hydrogen storage can meet the dynamic response requirements of the system, increasing the coupling ratio of solid and gaseous hydrogen storage capacity can further reduce the volume required for hydrogen storage.

The conclusions lay a theoretical foundation for optimizing the structural design of such MH-PCM tanks and offer guidance for improving the solid–gas coupling hydrogen storage performance. Future research can explore the dynamic response and hydrogen supply control issues in solid–gas coupled hydrogen storage, as well as determining the optimal coupling ratio between solid and gas for various applications. Additionally, future research should further conduct the experimental research to obtain more accurate performance evaluations, and expand the application scenarios of this novel hydrogen storage method.

### CRedit authorship contribution statement

**Yuhang Wang:** Software, Data curation, Writing – original draft, Writing – review & editing. **Hui Dai:** Resources, Validation, Writing – review & editing. **Zeqi Chen:** Validation, Writing – review & editing. **Suoying He:** Validation, Project administration. **Wenlong Wang:** Resources, Project administration. **Ming Gao:** Conceptualization, Methodology, Project administration, Supervision, Writing – review & editing.

### Declaration of Competing Interest

The authors declare that they have no known competing financial interests or personal relationships that could have appeared to influence the work reported in this paper.

### Data availability

Data will be made available on request.

### Acknowledgments

This paper is supported by the Natural Science Foundation of Guangdong Province (2023A1515012808) and Natural Science Foundation of Shandong Province (ZR2023ME025).

### References

- Abdin Z, Al Khafaf N, McGrath B, Catchpole K, Gray E. A review of renewable hydrogen hybrid energy systems towards a sustainable energy value chain. *Sustainable Energy Fuels* 2023;7:2042–62.
- Liu T, Yang Z, Duan Y, Hu S. Techno-economic assessment of hydrogen integrated into electrical/thermal energy storage in PV+ Wind system devoting to high reliability. *Energy Convers Manage* 2022;268.
- Jiang K, Wang P, Wang J, Liu N. Reserve cost allocation mechanism in renewable portfolio standard-constrained spot market. *IEEE Trans Sustainable Energy* 2022;13:56–66.
- Wang J, An Q, Zhao Y, Pan G, Song J, Hu Q, et al. Role of electrolytic hydrogen in smart city decarbonization in China. *Appl Energy* 2023;336.
- Zhang Y, Sun H, Tan J, Li Z, Hou W, Guo Y. Capacity configuration optimization of multi-energy system integrating wind turbine/photovoltaic/hydrogen/battery. *Energy* 2022;252.
- Wang Y, Li H, Feng H, Han K, He S, Gao M. Simulation study on the PEMFC oxygen starvation based on the coupling algorithm of model predictive control and PID. *Energy Convers Manage* 2021;249.
- Hosseini M, Dincer I, Naterer GF, Rosen MA. Thermodynamic analysis of filling compressed gaseous hydrogen storage tanks. *Int J Hydrogen Energy* 2012;37:5063–71.
- Raju M, Khaitan SK. System simulation of compressed hydrogen storage based residential wind hybrid power systems. *J Power Sources* 2012;210:303–20.
- Marino C, Nucara A, Panzera MF, Pietrafesa M, Varano V. Energetic and economic analysis of a stand alone photovoltaic system with hydrogen storage. *Renew Energy* 2019;142:316–29.
- Wang Y, Zhang H, Qi J, Han K, He S, Guo C, et al. Thermodynamic and exergy analysis of a novel PEMFC-ORC-MH combined integrated energy system. *Energy Convers Manage* 2022;264.
- Liu H, Xu L, Han Y, Chen X, Sheng P, Wang S, et al. Development of a gaseous and solid-state hybrid system for stationary hydrogen energy storage. *Green Energy Environ* 2021;6:528–37.
- Cui Y, Zeng X, Xiao J, Kou H. The comprehensive review for development of heat exchanger configuration design in metal hydride bed. *Int J Hydrogen Energy* 2022;47:2461–90.
- Bai X-S, Yang W-W, Tang X-Y, Dai Z-Q, Yang F-S. Parametric optimization of coupled fin-metal foam metal hydride bed towards enhanced hydrogen absorption performance of metal hydride hydrogen storage device. *Energy* 2022;243.
- Tong L, Xiao J, Yang T, Bénard P, Chahine R. Complete and reduced models for metal hydride reactor with coiled-tube heat exchanger. *Int J Hydrogen Energy* 2019;44:15907–16.
- Alqahtani T, Bamasag A, Mellouli S, Askri F, Phelan PE. Cyclic behaviors of a novel design of a metal hydride reactor encircled by cascaded phase change materials. *Int J Hydrogen Energy* 2020;45:32285–97.
- Li H, Wang N, He S, Gao M. Effect of inner-tube spacing on charging and discharging performance of latent energy storage heat exchangers. *Appl Therm Eng* 2022;216.
- Lewis SD, Chippar P. Analysis of heat and mass transfer during charging and discharging in a metal hydride - phase change material reactor. *J Storage Mater* 2021;33.
- Mellouli S, Ben Khedher N, Askri F, Jemni A, Ben Nasrallah S. Numerical analysis of metal hydride tank with phase change material. *Appl Therm Eng* 2015;90:674–82.
- El Mghari H, Huot J, Xiao J. Analysis of hydrogen storage performance of metal hydride reactor with phase change materials. *Int J Hydrogen Energy* 2019;44:28893–908.
- Tong L, Yuan Y, Yang T, Bénard P, Yuan C, Xiao J. Hydrogen release from a metal hydride tank with phase change material jacket and coiled-tube heat exchanger. *Int J Hydrogen Energy* 2021;46:32135–48.
- Tong L, Xiao J, Bénard P, Chahine R. Thermal management of metal hydride hydrogen storage reservoir using phase change materials. *Int J Hydrogen Energy* 2019;44:21055–66.
- Mellouli S, Abhilash E, Askri F, Ben Nasrallah S. Integration of thermal energy storage unit in a metal hydride hydrogen storage tank. *Appl Therm Eng* 2016;102:1185–96.
- Li H, Wang N, Zhao B, Feng H, Han K, He S, et al. Simulation study on the effect of fins on the heat transfer performance of horizontal dual-inner-tube latent thermal energy storage heat exchangers. *J Storage Mater* 2022;49.
- Dai H, Wang Y, Wang N, Li H, Gao M. Simulation study on charging performance of the latent energy storage heat exchanger with a novel conical inner tube. *J Storage Mater* 2022;56.
- Fang J, Han T, Bi Y, Yan H, Wei J. Numerical study on heat transfer and enhancement mechanism in PCM-filled shell-and-tube heat exchangers. *Front Energy Res* 2022;10.
- Bellos E, Lykas P, Tzivanidis C. Performance analysis of a zero-energy building using photovoltaics and hydrogen storage. *Applied System Innovation* 2023;6.
- Bovo A, Poli N, Trovò A, Marini G, Guarnieri M. Hydrogen energy storage system in a Multi-Technology Microgrid: technical features and performance. *Int J Hydrogen Energy* 2023;48:12072–88.
- Sharma R, Srinivasa Murthy S, Dutta P, Rao BS. Performance of solid state hydrogen storage assisted standalone polygeneration microgrids for various climatic zones of India. *Energy* 2022;258.
- Kumar K, Alam M, Verma S, Dutta V. Analysis of metal hydride storage on the basis of thermophysical properties and its application in microgrid. *Energy Convers Manage* 2020;222.
- Alqahtani T. Performance evaluation of a solar thermal storage system proposed for concentrated solar power plants. *Appl Therm Eng* 2023;229.
- Jemni A, Nasrallah SB, Lamloumi J. Experimental and theoretical study of a metal-hydrogen reactor. *Int J Hydrogen Energy* 1999;24:611–44.
- Mellouli S, Askri F, Abhilash E, Ben Nasrallah S. Impact of using a heat transfer fluid pipe in a metal hydride-phase change material tank. *Appl Therm Eng* 2017;113:554–65.
- Kong L, Yu J, Cai G. Modeling, control and simulation of a photovoltaic /hydrogen/ supercapacitor hybrid power generation system for grid-connected applications. *Int J Hydrogen Energy* 2019;44:25129–44.
- Cho J-H, Yu S-S, Kim M-Y, Kang S-G, Lee Y-D, Ahn K-Y, et al. Dynamic modeling and simulation of hydrogen supply capacity from a metal hydride tank. *Int J Hydrogen Energy* 2013;38:8813–28.
- Chung CA, Ho C-J. Thermal–fluid behavior of the hydriding and dehydriding processes in a metal hydride hydrogen storage canister. *Int J Hydrogen Energy* 2009;34:4351–64.
- Zhu D, Ait-Amirat Y, N'Diaye A, Djerdir A. Active thermal management between proton exchange membrane fuel cell and metal hydride hydrogen storage tank considering long-term operation. *Energy Convers Manage* 2019;202.
- Ben Mâad H, Miled A, Askri F, Ben Nasrallah S. Numerical simulation of absorption-desorption cyclic processes for metal-hydrogen reactor with heat recovery using phase-change material. *Appl Therm Eng* 2016;96:267–76.



- [38] Ye Y, Lu J, Ding J, Wang W, Yan J. Numerical simulation on the storage performance of a phase change materials based metal hydride hydrogen storage tank. *Appl Energy* 2020;278.
- [39] Zhang Y, Wei W. Model construction and energy management system of lithium battery, PV generator, hydrogen production unit and fuel cell in islanded AC microgrid. *Int J Hydrogen Energy* 2020;45:16381–97.
- [40] Wang Y, Zhang H, He S, Wang W, Gao M, Koltsova E, et al. Dynamic analysis and control optimization of hydrogen supply for the proton exchange membrane fuel cell and metal hydride coupling system with a hydrogen buffer tank. *Energ Conver Manage* 2023;291.
- [41] Jensen JO, Vestbø AP, Li Q, Bjerrum NJ. The energy efficiency of onboard hydrogen storage. *J Alloy Compd* 2007;446–447:723–8.